A gyro-Landau-fluid transport model

R. E. Waltz, G. M. Staebler, W. Dorland,[a] G. W. Hammett,[b] M. Kotschenreuther,[a] and J. A. Konings[c]
General Atomics, P.O. Box 85608, San Diego, California 92186-5608

(Received 7 February 1997; accepted 3 April 1997)

A physically comprehensive and theoretically based transport model tuned to three-dimensional (3-D) ballooning mode gyrokinetic instabilities and gyrofluid nonlinear turbulence simulations is formulated with global and local magnetic shear stabilization and $E\times B$ rotational shear stabilization. Taking no fit coefficients from experiment, the model is tested against a large transport profile database with good agreement. This model is capable of describing enhanced core confinement transport barriers in negative central shear discharges based on rotational shear stabilization. The model is used to make ignition projections from relative gyroradius scaling discharges. © *1997 American Institute of Physics.* [S1070-664X(97)01407-9]

I. INTRODUCTION

A comprehensive and practical fast dispersion theoretic transport model has been developed that can be tuned to approximate the linear growth rates of a three-dimensional (3-D) ballooning mode gyrokinetic stability (GKS) code[1] and the transport coefficients of 3-D nonlinear gyro-Landau-fluid (GLF) simulations.[2–4] As a purely theoretical model, it takes no fitting coefficients from experiments. The model contains global magnetic shear ($\hat{s}$) as well as local shear or Shafranov shift (α) stabilization. It also contains $E\times B$ rotational shear stabilization as well as parallel velocity shear destabilization.

It is difficult to accurately and comprehensively capture the parametric dependencies of theoretically based numerical simulations of turbulent transport with simple algebraic formulas. Here we take a dispersion theoretic approach combined with quasilinear theory and a novel mixing rule. The model consists of a linear eigenvalue system obtained from an eightfold set of reduced [one-dimensional (1-D)] GLF perturbed moment equations of motion. The eigenvalue problem is solved at each plasma radius for all linear growth rates. Quasilinear electron and ion energy, particle, and toroidal momentum flows, as well as turbulent $e-i$ energy exchange, are then obtained from the phase relation between the perturbed moment eigenvectors and the perturbed $E\times B$ velocity. The toroidal ion temperature gradient (ITG) mode, the collisionless to dissipative trapped electron drift modes, and the ideal magnetohydrodynamic (MHD) ballooning modes, as well as the edge resistive modes, are included. The model contains finite-β electromagnetic effects. Fast ion and impurity stabilization is retained through ion dilution. (Generalization to include impurity flows and dynamics is also given.) We have taken the passing electrons to be massless and isothermal but have retained resistivity for the edge modes. The model is formulated for an $\hat{s}-\alpha$ shifted circle equilibrium. Elongation is considered only with the working hypothesis that all plasma gradients are taken along the average minor axis (d/dr), where $r=(R_{\rm in}+R_{\rm out})/2$.

The mixing length rule used to normalize the perturbed $E\times B$ velocity ($\tilde{\nu}_{E\times B}$) in the quasilinear flows is a distinguishing feature of the model. The nonlinear saturation (as applied to each of ten modes in a k_y spectrum and all unstable dispersion theory roots or branches) is given by the mixing rule rate $\tilde{\nu}_{E\times B}\cdot k_{xM}\sim\gamma_{\rm net}^{\hat{\alpha}}\gamma_d^{(1-\hat{\alpha})}$, where $\gamma_{\rm net}$ is the net growth rate of the leading ballooning modes after accounting for rotational shear stabilization and γ_d is the damping rate of a representative $n=0$ radial mode ($k_y=0$, $k_x'\neq 0$) that can be approximated by the ion curvature drift frequency of the corresponding finite-n ballooning mode. (For the ballooning modes, k_x' refers to the ballooning mode angle θ_0 label $k_x'=\hat{s}k_y\theta_0$.) Here k_{xM} is the mixing cross-field wave number scaled to the ion gyroradius $k_{xM}^2=k_y^2+\hat{\beta}k_x^2$. $\hat{\alpha}=\frac{1}{2}$, and $\hat{\beta}=0$ are tuned to fit the 3-D GLF nonlinear simulations. In the simple limit of retaining only the $E\times B$ motions, it is easily shown that this novel mixing rule results in a quasilinear ion heat diffusivity $\chi\approx\frac{3}{2}(\gamma_{\rm net}/k_{xM}^2)\cdot\gamma_d\gamma/(\gamma^2+\omega_0^2)$ with the dependence on radial mode damping and saturation with temperature gradient seen in recent adiabatic electron ITG mode simulations.[2,3] The nonlinear simulations[2] have shown that $E\times B$ rotational shear stabilization of transport can be approximately described by setting $\gamma_{\rm net}=\gamma-\gamma_E-\gamma^*$, where γ is the drift-ballooning mode growth rate in the absence of rotational shear, $\gamma_E\approx(r/q)d(qV_{E\times B}/r)/dr$ is the $E\times B$ (or Doppler shift) rotational shear rate, γ^* is a diamagnetic rotational shear rate associated with other profile variations over the modes. It is likely associated with the drift mode rotation in the absence of $E\times B$, but we shall generally ignore it in applications of the model. Unlike the ballooning mode rate γ that is independent of $\rho^*=(\rho_s/a)$ for k_y and $k_x\propto 1/\rho_s$, diamagnetically induced γ_E (and γ^*) increase with ρ^* breaking the otherwise gyro-Bohm scaling of the transport coefficients. Transport coefficients can decrease going to small ρ^* and also going to large ρ^*, even to the point of stability where $\gamma_{\rm net}=0$. Thus, schematically, in the absence of $E\times B$ rotation induced by toroidal rotation V_ϕ, the $E\times B$ velocity becomes comparable to the diamagnetic velocity and $\gamma_E\propto\rho^*$, we have $\chi\propto\chi_{\rm Bohm}\cdot\rho^*(1-\rho^*/\rho^*_{\rm crit})$ with $\rho^*_{\rm crit}\propto\gamma$. Thus, χ has a distinctly nonpower law dependence on ρ^*. While this picture was developed from nonlinear ballooning mode simulations (in a local cyclic annulus) with $E\times B$ shear linearly

[a]Also at the Institute for Fusion Studies, University of Texas.
[b]Also at the Princeton Plasma Physics Laboratory.
[c]Also at FOM, The Netherlands.

 1070-664X/97/4(7)/2482/15/$10.00

coupling the ballooning modes at different k_x',[2] the breaking of gyro-Bohm scaling near the threshold by diamagnetic shear stabilization and with correlation lengths continuing to scale with the local gyroradius ρ_s is fully consistent with recent two-dimensional (2-D) full radius toroidal simulations.[5]

This paper was clearly motivated by the early success of the Institute for Fusion Studies—Princeton Plasma Physics Laboratory (IFS-PPPL) formula-based gyrofluids model.[6] The present dispersion theoretic model is more comprehensive, in that it includes a complete description of plasma, impurity, and toroidal momentum transport as well as energy exchange; the trapped electron branch as well as finite beta (ideal MHD) physics, resistive edge modes, and high-k η_e modes; reverse shear ($\hat{s}<0$) and Shafranov shift (α) stabilization; parallel velocity shear destabilization; and most importantly, $E\times B$ rotational shear stabilization allowing transport bifurcations. However, apart from tokamak discharges where these effects are clearly important and in limits (abstract or otherwise) where they are not, it is difficult to characterize the present dispersion theoretic model as overall more faithful to the underlying gyrokinetic linear stability and gyrofluid nonlinear simulations. Both models are approximations with one model tracking the underlying theory at one point better than at others, and vice versa.

The outline of the paper is as follows: a detailed formulation of the model is given in Sec. II. It focuses on the use of an along the field line trial ballooning mode function, whose width is parametrized in $\hat{s}$ and q, to obtain reduced GLF dispersion equations. The quasilinear flow relations are given in terms of these reduced linear dispersion equations and the rotational shear rates used are precisely defined. In Sec. III we illustrate how well the reduced dispersion fits the linear growth rates obtained from the 3-D GKS code[1] as well as how the model is normed to the 3-D GLF nonlinear simulations.[2–4] Comparisons with the IFS-PPPL model[6] are given. In Sec. IV we give an abstract illustration of the rotational stabilization transport bifurcations implicit in the model. Such bifurcations are a mixture of the heat flow type in which diamagnetically induced rotational stabilization leads to a decrease in heat flow with increasing temperature gradient; and a momentum type, in which a spin-up arises from toroidally driven rotational stabilization leading to decreased toroidal momentum flow at increasing rotational shear. The bifurcations from diamagnetically induced rotational stabilization have a very poor power threshold scaling to smaller ρ^*. In Secs. V and VI, we demonstrate the use of a fast ''shooting'' transport code[7] with boundary conditions on temperatures given at the 90% toroidal flux radius to test the model against experiments. The density profiles and rotational profiles are taken from the experiment. Although the model specifies plasma and momentum transport, self-consistent treatment of these channels and, particularly, following transport dynamically through a bifurcation is left to future work. Since rotational shear stabilization is a distinguishing feature of this model, we first apply the model in Sec. V to an instantaneous transport analysis of the DIII-D[8] core transport barrier in a negative central shear (NCS) discharge.[9] We argue that $E\times B$ rotational shear induced by a momentum channel bifurcation is the most likely cause of the core transport barrier. The model is then tested against a wide range of Low- (L-) and High- (H-) mode discharges in the International Thermonuclear Experimental Reactor (ITER)[10] transport profile database[11] with a good degree of correlation in Sec. VI. The correlation is compared to that for the IFS-PPPL model[6] and global scaling laws (GSL). In Sec. VII, we single out tests of the model against the DIII-D dimensionally similar ρ^* scaling experiments,[12] which are then projected to ignition in ITER. Finally, some key results and future directions are summarized in Sec. VIII.

II. FORMULATION OF THE MODEL

The model closely follows the four-moment GLF equations given in Ref. 2, with the exception that we have assumed resistive but massless (no inertial) isothermal passing electrons. In detail, these equations of motion correspond to gyrofluid moments for the relative perturbed gyrocenter ion densities (N_{i_k}) and pressures ($P_{i\|_k}$, $P_{i\perp_k}$), ion parallel velocity (U_{i_k}), trapped electron density (N_k^t) and pressure (P_k^t), untrapped or passing electron density (N_k^u), and parallel magnetic vector potential (A_k),

$$-i\omega N_{i_k}=-i\omega*[(1_i-\eta_i)\phi_{1k}+\eta_i\phi_{2k}]+i\omega_D\phi_{12k}-ik_\|U_{i_k}+i\omega_{Di}\tau^{-1}(\tfrac{1}{2})(P_{i\|_k}+P_{i\perp_k}), \tag{1}$$

$$-i\omega P_{i\|_k}=-i\omega*(1_i\phi_{i_{1k}}+\eta_i\phi_{i_{2k}})+iX_\|\omega_D\phi_{i_{12k}}-ik_\|(\Gamma_\|U_{i_k}-i\sigma_s\chi_{\|1_i}T_{i\|_k})+i\omega_{Di}\tau^{-1}[X_\|P_{i\|_k}+(\tfrac{3}{2})T_{i\|_k}+(\tfrac{1}{2})T_{i\perp_k}-i\sigma_t(\nu_\|^\|T_{i\|k}+\nu_\perp^\|T_{i\perp k})], \tag{2}$$

$$-i\omega P_{i\perp_k}=-i\omega*[(1_i-\eta_i)\phi_{i_{2k}}+2\eta_i\phi_{i_{3k}}]+iX_\perp\omega_D\phi_{23k}-ik_\|(\Gamma_\perp U_{i_k}-i\sigma_s\chi_{1_i}^\perp T_{i\perp_k})+i\omega_{Di}\tau^{-1}[X_\perp P_{i_{\perp k}}+T_{i_{\perp k}}+(\tfrac{1}{2})T_{i\|_k}-i\sigma_t(\nu_\|^\perp T_{i\|_k}+\nu_\perp^\perp T_{i\perp_k})], \tag{3}$$

$$-i\omega m_iU_k=-ik_\|(\tau^{-1}P_{i\|_k}+Z_i\phi_{i_{1k}})-ik_y\gamma_P\phi_k+i\omega_{Di}[(\tfrac{1}{2})(\Gamma_\|+\Gamma_\perp)U_{i_k}+i\sigma_t\mu U_{i_k}]-(\beta_e/2)[Z_i(-i\omega A_k)-i\omega*(1_iA_{1k}+\eta_iA_{2k})], \tag{4}$$

$$-i\omega N_k^t=-i\omega*\sqrt{\epsilon}1_e\phi_k+i(\tfrac{3}{4})\omega_D\sqrt{\epsilon}\phi_k+i\omega_D(\tfrac{3}{4})P_k^t-(\nu_{ei}/\epsilon)[(1-\sqrt{\epsilon})(F_{nn}N_k^t+F_{np}P_k^t)-\sqrt{\epsilon}F_{nf}N_k^u], \tag{5}$$

$$-i\omega P_k^t = -i\omega^* \sqrt{\epsilon}(1_e+\eta_e)\phi_k + i(\tfrac{5}{4})\omega_D\sqrt{\epsilon}\phi_k + i\omega_D[(\tfrac{5}{4})P_k^t + \zeta_D(P_k^t - N_k^t)] - (\nu_{ei}/\epsilon) \times[(1-\sqrt{\epsilon})(F_{pn}N_k^t + F_{pp}P_k^t) - \sqrt{\epsilon}F_{pf}N_k^u], \tag{6}$$

$$-i\omega N_k^u = -i\omega_*(1-\sqrt{\epsilon})1_e\phi_k + i(\tfrac{3}{4})\omega_D(1-3/4\sqrt{\epsilon})\phi_k - i\omega_D(\tfrac{3}{4})(N_k^u + T_k^u) - ik_\parallel(U_k - k_\perp^2 A_k) + (\nu_{ei}/\epsilon)[(1-\sqrt{\epsilon})(F_{nn}N_k^t + F_{np}P_k^t) - \sqrt{\epsilon}F_{nf}N_k^u], \tag{7}$$

$$-i\omega A_k = -i\omega_* 1_e A_k + ik_\parallel(\beta_e/2)[N_k^u/(1-\sqrt{\epsilon}) - \phi_k] - (2/\beta_e)m_e\nu_{ei}k_\perp^2 A_k. \tag{8}$$

The relative ion temperature perturbations are given by $T_{i\parallel_k} = P_{i\parallel_k} - N_{ik}$ and $T_{i_{\perp k}} = P_{i_{\perp k}} - N_{i_k}$, and the passing electron relative temperature perturbations follow from the isothermal condition $T_k^u = [(\beta_e/2)\omega^*/k_\parallel]\eta_e A_k$. Quasineutrality $\Sigma_i Z_i w_i N_k - N_k^u - N_k^t = \Sigma_i Z_i^2 w_i \tau(1-\phi_{i_{lk}})$ relates the densities to the electrostatic potential (ϕ_k), where $\phi_{i_{jk}} = g_{ij}\phi_k$ with $g_{ij} = 1/(1+b_i)^j$ a Padé approximate to the gyro-Bessel functions, and $b_i = (m_i/Z_i^2)\tau^{-1}k_\perp^2$ is the finite Larmor radius parameter. Here $k_\perp^2 = k_y^2 + k_x^2$ and $[\phi_{ij} = (\phi_i + \phi_j)/2]$. Also, $\tau^{-1} = T_i/T_e$, Z_i is the charge on the ion relative to the main ion, and m_i and m_e are the ion and electron mass relative to the main ion. In addition, $w_i = n_i/n_e$ is the ion density weight. If full average impurity ion dynamics are used with 12 in place of 8 equations, then the sum Σ_i over the main ion ($Z_i = 1$, $m_i = 1$) and average impurity ion is needed. Here β_e is the electron beta, $\sqrt{\epsilon}$ is the fraction of trapped electrons, and ν_{ei} is the electron–ion collision rate. The energy-dependent detrapping–retrapping collision operators[13] are constructed from energy bin fractions, giving the same first and second moments as a Maxwellian: $F_{nn} = [(t_h/t_c)^{3/2} - (t_c/t_h)^{3/2}]/[t_h - t_c]$, $F_{np} = (3/2)[(1/t_h)^{3/2} - (1/t_c)^{3/2}]/[t_h - t_c]$, $F_{nf} = (f_h/t_h)^{3/2} + (f_c/t_c)^{3/2}$, $F_{pn} = (2/3)[(t_h/t_c)^{1/2} - (t_0/t_h)^{1/2}]/[t_h - t_c]$, $F_{pp} = [(1/t_h)^{1/2} - (1/t_c)^{1/2}]/[t_h - t_c]$, and $F_{pf} = (\tfrac{2}{3})[(f_h/t_h)^{1/2} + (f_0/t_c)^{1/2}]$, where $t_h = 4.08$, $t_c = 0.918$, $f_h = 0.184$, and $f_c = 0.816$. Detailed balance and particle conservation are satisfied by the collision model and the trapped electron response becomes adiabatic (for passing electrons adiabatic) at large ν_{ei}. The GLF closure involves several fit coefficients $\chi_1^\parallel = 2\chi_1^\perp = (\sqrt{2})2/\sqrt{\pi m_i}$ for parallel motion and $\mu = (0.80 - 0.57i\sigma_t)$, $\nu_\parallel^\parallel = \nu_\perp^\perp = (1 - i\sigma_t)$, $\nu_\perp^\parallel = \nu_\parallel^\perp = 0$ for curvature motion (with $\sigma_s = k_\parallel/|k_\parallel|$, $\sigma_t = \omega_D/|\omega_D|$). The electron curvature drift frequency is $-\omega_D$, and $\omega_{i_D} = \omega_D/Z_i$, and ω^* is the drift frequency for electrons at unit density gradient length. The adiabatic compression indices are $\Gamma_\parallel = 3$, and $\Gamma_\perp = 1$, $X_\parallel = 2$, $X_\perp = 3/2$. $\zeta_D = -0.7 + 0.8i\sigma_t$.

We use a system of normalized units from Ref. 2 and earlier papers in which the macrolength is in units of a, the plasma toroidal flux radius $\rho(a)$. The cross-field wave numbers (k_y and k_x) in inverse gyrounits $1/\rho_s$, where $\rho_s = c_s/\Omega_i$ with $c_s = (T_e/M_i)^{1/2}$, $\Omega_i = eB/M_i c$. The driving electron (ion) density and temperature gradients are $1_{e(i)} = a/L_{ne(i)}$ and $\eta_{e(i)} = a/L_{Te(i)}$, where, for example, $1/L_T = d\ \ln T/dr$ with $r = (R_{\rm out} + R_{\rm in})/2$ as the average minor radius. All rates and frequencies are in units of c_s/a and velocities are in units of c_s. Thus the parallel (or toroidal) velocity shear driving rate is given by $\gamma_p = dV_\parallel/dr/[c_s/a]$. (Note $dV_\parallel/dr \approx dv_\phi/dr$.) In these units, $\omega^* = k_y$ and linear growth rate (γ) and frequency (ω_0) of any mode is obtained from $-i\omega = \gamma - i\omega_0$.

In terms of the ballooning mode extended angle θ, the curvature drift frequency in our units is $\omega_D = k_y(2/R)[\cos\theta + (\hat{s}\theta - \alpha\sin\theta)\sin\theta]$, the square radial wave number is $k_x^2 = k_y^2(\hat{s}\theta - \alpha\sin\theta)^2$, and the parallel wave number is $k_\parallel = (a/Rq)i\partial/\partial\theta$. To reduce these equation to one dimension, we introduce even and odd Gaussian trial functions $(\Theta_e, \Theta_0) = [1, (i\theta/\theta_{\rm rms})]\int \exp(-\theta^2/40_{\rm rms}^2)$ and weighted averages $\langle F\rangle = \int d\theta\ F\Theta_e^2/\int d\theta\ \Theta_e^2$, $\langle F\rangle_{e0} = \int d\theta\ F\Theta_0 \int d\theta\ \Theta_0^2$. The ion parallel velocity U_{ik} moment and A_k vector potential are odd moments and the other moments are even. Multiplying the equations by the appropriate trial function and averaging along the field line, θ-dependent quantities become simple numbers: $\omega_D \Rightarrow \langle\omega_D\rangle$; $k_x^2 \Rightarrow \langle k_x^2\rangle$; $k_\parallel \Rightarrow \hat{k}(a/Rq)\langle i\partial/\partial\theta\rangle_{e0} = \hat{k}(a/Rq)/(2\theta_{\rm rms})$; and the trapping fraction is taken to be $\sqrt{\epsilon} = \hat{e}\{(r/R)[1 + \langle\cos(\theta)\rangle]/[1 + r/R\langle\cos(\theta)\rangle\}^{1/2}$, where we have introduced two fit coefficients $\hat{k}$ and $\hat{e}$. By making the inverse ballooning mode width $1/\theta_{\rm rms}$, a linearly increasing function of q and of shear $\hat{s}$, as it does physically, we are able to obtain very good fits to a 3-D GKS code with tuning factors $\hat{k}$ and $\hat{e}$ near unity. Physically $1/\theta_{\rm rms}$ is also an increasing function of β, but better fits to the GKS code are obtained by an enhancement factor on β_e: $\beta_e \Rightarrow \beta_e/(1+\hat{b}^2)$, where $\hat{b}$ is another fit coefficient. When parallel velocity shear γ_P enters in Eq. (4), parity is broken and the trial functions become mixed with an admixture strength $(-\gamma_P\alpha_n)$. *The γ_P term in Eq. (4) acquires the factor $(-\gamma_P\alpha_n)$ when dispersion equations are appropriately averaged over the mixed parity trial functions, making the final dispersion relations dependent on γ_P^2.* Since γ_P is in units of c_s/a and the equations can only depend on Rq in the slab limit, α_n must scale as $\alpha_P(a/Rq)$, where α_P is a tuning coefficient to match γ_P-driven growth rates from the GKS code.

We note here that there are two simpler alternatives to full average impurity ion dynamics. The first is to assume the impurities do not respond to the perturbed potential at all (like the fast ions) so that their only effect is to dilute the contributions of the main ions (ion weight defined above $w_i < 1$). The second goes beyond the simple dilution model to assume that the impurities respond only to $E\times B$ convection $N_{ik} = \{-i\omega^*[(1_i - \eta_i)\phi_{1k} + \eta_i\phi_{2k}] + i\omega_D\phi_{12k}\}/(\gamma - i\omega_0)$, $P_{i\parallel_k} = [-i\omega^*(1_i\phi_{i_{1k}} + \eta_i\phi_{i_{2k}}) + iX_\parallel\omega_D\phi_{i_{12k}}]/(\gamma - i\omega_0)$, and $P_{i\perp k} = \{-i\omega^*[(1_i - \eta_i)\phi_{i_{2k}} + 2\eta_i\phi_{i_{3k}}] + iX_\perp\omega_D\phi_{23k}\}/(\gamma - i\omega_0)$. The simpler models show the generally stabilizing effect of impurities but only roughly approximates the full dynamics. On the other hand, it is not easy to get reliable data on impurity density gradients so, in practice, we have used the simple dilution model.

For every k_y (at $k_x' = 0$) and unstable root of the disper-

sion relations, Eqs. (1)–(8), we obtain the transport diffusivities from quasilinear relations. The sum over these contributions is made with the operation Σ_k to be defined below. The effective ion particle diffusivity is

$$D^i_{\rm eff}=[c_s(\rho_s^2/a)]\sum_k \ {\rm Re}[N^*_{ik}(-ik_y\phi_k)/ (|\phi_k/\phi_M|)^2]/(a/L_{ni}), \tag{9a}$$

which is to be used with the ion diffusion equation

$$\partial n_i/\partial t=-1/V'\ \partial/\partial\rho\ V'\langle|\nabla\rho|\rangle(d\rho/dr)D^i_{\rm eff}\ \partial n_i/\partial\rho. \tag{9b}$$

The effective ion *energy* diffusivity is

$$\chi^i_{\rm eff}=c_s(\rho_s^2/a)]\sum_k \ {\rm Re}\{(3/2)[(1/3)P_{i\|_k}+(2/3)P_{i_{\perp k}}]^* \times(-ik_y\phi_k)/(|\phi_k/\phi_M|)^2\}/(a/L_{Ti}), \tag{10a}$$

which is to be used with the ion energy diffusion equation,

$$\partial(3/2)\sum_i \ n_i\ T_i/\partial t=-1/V'\ \partial/\partial\rho\ V'\langle|\nabla\rho|\rangle \times(d\rho/dr)\sum_i \ n_i\chi^i_{\rm eff}\ \partial T_i/\partial\rho+\Delta_{ei}. \tag{10b}$$

The effective electron *energy* diffusivity is

$$\chi^e_{\rm eff}=c_s(\rho_s^2/a)]\sum_k \ {\rm Re}[(3/2)(P^t_k+N^u_k+T^u_k)^* \times(-ik_y\phi_k)/(|\phi_k/\phi_M|)^2]/(a/L_{Te}), \tag{11a}$$

which is to be used with the electron energy diffusion equation,

$$\partial(3/2)n_e\ T_e/\partial t=-1/V'\ \partial/\partial\rho\ V'\langle|\nabla\rho|\rangle \times(d\rho/dr)n_e\chi^e_{\rm eff}\ \partial T_e/\partial\rho-\Delta_{ei}. \tag{11b}$$

The turbulent electron to ion energy exchange is

$$\Delta_{ei}=\sum_i \ (n_iT_ec_s/a(\rho_s/a)^2)Z_i \times\sum_k \ {\rm Re}\left((i\omega_0N^*_{ik}\phi_k)/(|\phi_k/\phi_M|)^2\right) \approx\sum_i \ T_eL^{-1}_{ni}(-\omega_0/\omega^*)Z_i\Gamma_i, \tag{11c}$$

where Γ_i is the ion flux. Note that it is pointless to break up energy diffusion into conductive and convective parts for turbulent transport. There is no unambiguous division, although one could refer to $[(\frac{3}{2})T_iD^i_{\rm eff}\ \partial n_i/\partial\rho]/(n_i\chi^i_{\rm eff}\ \partial T/\partial\rho)$ as the convective fraction of the ion energy flow, for example. In practice, the anomalous exchange is of little importance unless convective loses are large. The toroidal momentum diffusivity is given by $\eta^\phi_{\rm eff}=\eta_\|+(B_\theta/B_\phi)\eta_\perp$ to be used in the momentum diffusion equation,

$$M_in_i\ \partial V_\phi/\partial t=-1/V'\ \partial/\partial\rho\ V'\langle|\nabla\rho|\rangle \times[(d\rho/dr)M_in_i\eta^\phi_{\rm eff}\ \partial V_\phi/\partial\rho+M_iv_\phi\Gamma], \tag{12a}$$

where the perpendicular and parallel viscosities are

$$\eta_\perp=[c_s(\rho_s^2/a)]\sum_k \ {\rm Re}\langle(-k_yk_x\phi_k)^*\{\phi_k+\tau^{-1}[(1/3)P_{i\|_k} +(2/3)P_{i_{\perp k}}]\}(-\alpha_n)/(|\phi_k/\phi_M|)^2\rangle, \tag{12b}$$

$$\eta_\|=[c_s(\rho_s^2/a)]\sum_k \ {\rm Re}(U^*_{ik}(-ik_y\phi_k)(-\alpha_n)/(|\phi_k/\phi_M|)^2). \tag{12c}$$

The direct quasilinear calculation of $\eta_\|$ leads to negative values at low values of rotational shear rate γ_P, possibly because we have not found an accurate treatment of the parity breaking in the trial functions. To avoid what we take to be an unphysical result, we have substituted only the linear $E\times B$ terms for $U_k\approx-ik_y\gamma_P(-\gamma_P\alpha_n)\phi_k/(\gamma-i\omega_0)$ in Eq. (12c), making $\eta_\|$ manifestly positive. In all the above diffusion equations, we must add the appropriate sources, neoclassical diffusion, and the classical electron-to-ion energy exchange to the right-hand sides. Here ρ is the toroidal flux radius defined by $\Phi=B_\phi\pi\rho^2$. In addition, r is the average minor radius, as defined earlier. The factors $\langle|\nabla\rho|\rangle(d\rho/dr)$ account for the proper surface-to-volume ratio under the assumption that transport is driven by d/dr gradients.

To normalize the quasilinear transport coefficients, we write the mixing rule rate $\tilde{\nu}_{E\times B}\cdot k_{xM}\sim\gamma^{\hat\alpha}_{\rm net}\gamma_d^{(1-\hat\alpha)}$. A mixing rule rate $\gamma^{3/4}_{\rm net}\gamma_d^{1/4}$ gives a better description of the radial mode dependence and $\gamma^{1/4}_{\rm net}\gamma_d^{3/4}$ better describes the extreme temperature gradient saturation. We have taken a compromise $\hat\alpha=\frac{1}{2}$ that better describes the threshold and the dependence of χ on $\gamma_{\rm net}$. In the normalized form,

$$\phi_M=\gamma^{1/2}_{\rm net}\gamma_d^{1/2}/(k_{xM}k_y), \tag{13}$$

where $\gamma_d=0.2(3/2)|\omega_D|\tau^{-1}$ approximates the damping of an $n=0$ radial mode with k'_x equal to k_y of the high-n mode. Here $k^2_{xM}=k^2_y+\hat\beta k^2_x$, and since $k^2_x\propto\hat s^2$, $\hat\beta$ can be used to tune the dependence of diffusivity on $\hat s$. Also, $\hat\beta=0$ gives a better description of the shear dependence than $\hat\beta=1$ and, indeed, if k^2_{xM} were weighted totally to k^2_x, the diffusion at $\hat s=0$ would be infinite. *We stress that this parametrization of the mixing rate rule is by no means unique and is only a heuristic recipe attempting to best approximate the results of 3-D GLF simulations*. The summation Σ_k over all unstable modes (j) with $\gamma_{\rm net}>0$ and a logarithmic spectrum of N modes with $k_y(n)$ from k_m to k_M $\{k_y(n)=k_M\ \exp[-\ln(k_M/k_m)(n/N-1)/(1/N-1)]\}$ is defined by

$$\Sigma_kF_k=C\sum_{n=1}^N \ k_y(n)(\Sigma_jF_{nj})\ \Big/\ \sum_{n=1}^N \ k_y(n), \tag{14}$$

where C is a single-model norm coefficient used to fit $\chi^i_{\rm eff}$ from the 3-D gyrofluid simulations of ITG transport with adiabatic electron physics.

There is an additional contribution to the electron heat diffusivity from the very high k_y η_e modes. We take advantage of the complete isomorphism between this contribution and ITG (or η_i) mode turbulence with adiabatic electrons ($\sqrt{\epsilon}\to 0$ and $\beta\to 0$ for inertia-free electrons) merely switching e and i labels on Eq. (10a) and correspondingly in the dispersion relations Eqs. (1)–(8). No new fit or tuning parameters are introduced. Since the growth rates for the η_e modes far exceeds the rotational shear rates, $\gamma_{\rm net}$ is simply the ballooning mode rate γ for these modes. The contribution from the η_e modes is of no importance, except when the low-k modes are completely stabilized by rotational shear.

The net growth rate formulation requires some discussion and a definition of the $E\times B$ or Doppler rotational shears in relation to other rotational shear rates. It should be made clear that the stabilization condition $\gamma_{\rm net}=\gamma-\alpha_E\gamma_E-\alpha^*\gamma^*$ is a provisional one based on nonlinear 3-D GLF simulations[2] showing that the ITG turbulent transport vanishes at a critical $E\times B$ shear rate $\gamma_E=\gamma_{\max}/\alpha_E$, where $0.5<\alpha_E<1.5$. The general parametric dependence of α_E is uncertain, but it is known that there is no evidence that $\alpha_E\propto 1/\hat{s}$ at vanishing $\hat{s}$, as might be expected from the convection of ballooning modes in the ballooning angle.[2] We have taken α_E equal to 1, but it is clear that a more precise knowledge of the critical $E\times B$ shear rate is needed. Furthermore, it should be clear that when the $E\times B$ shear rates become comparable to the diamagnetic rotational shear rates, other diamagnetic level rotational shear rates γ^* will enter the problem. Although it is clear that these rates are diamagnetic with proportionality to ρ^*, we can only speculate that γ^* may be shear in the intrinsic mode phase speed so that combined with γ_E (at $\alpha^*=\alpha_E$), it is the shear in the total mode phase velocity that stabilizes the turbulence. Generally, we have ignored these poorly known rates setting $\alpha^*=0$. Since we sum over a spectrum of modes, $\gamma_{\max}=\gamma_E$ appears as our stability condition (with γ_E converted to c_s/a rate units).

It is worth noting that the factor q/r factors appear in our definition[2] of the operative $E\times B$ shear rate,

$$\gamma_E\approx (r/q)d(qV_{E\times B}/r)/dr, \tag{15}$$

because the $E\times B$ velocity enters the ballooning mode equations as $(m/r)V_{E\times B}=(nq/r)V_{E\times B}$ and the toroidal mode number n is the proper model label. We have interpreted this simple circular formula for real geometry by assuming that the gradient is along the midplane or average minor radius r and further that γ_E is constant on a flux surface. This is consistent with the assumptions of the simulations and the interpretation of the driving gradients.

We have used simple circular formulas for obtaining $V_{E\times B}$ in terms of V_ϕ and the neoclassical V_θ:

$$V_{E\times B}=\tau^{-1}\rho^* c_s(1_i+\alpha_{1\rm neo}\eta_i)-\sigma(r/Rq)V_\phi, \tag{16a}$$

$$V_\parallel=\sigma V_\phi+\tau^{-1}\rho^* c_s[(\alpha_{1\rm neo}^{-1})\eta_i](r/Rq), \tag{16b}$$

where $\sigma=+(-)$ for co- (counter-) rotation. Here V_ϕ is the plasma toroidal rotation that must be corrected by diamagnetic terms from the given experimental impurity rotation $V_{\phi I}$,

$$V_\phi=V_{\phi I}+\alpha_{2\rm neo}3/2\tau^{-1}\rho^* c_s\eta_i(r/Rq). \tag{16c}$$

The collisionless banana regime coefficients[14] are $\alpha_{1\rm neo}=1-0.8839f/(0.3477+0.4058f)$, $\alpha_{2\rm neo}=(1-f)/(1+1.1671f)$, and $f=1-1.46(r/R)^{1/2}+0.46(r/R)^{3/2}$

Before leaving the formulation of γ_E, we should note that there is considerable uncertainty in interpreting the simulations for real geometry. Here γ_E can also be written[15] as $(cRB_\theta/B)d(E_r/B_\theta R)/dr$, which becomes, in the limit of pure toroidal rotation, $RB_\theta/B(d\Omega/dr)$. Also, $E_r/B_\theta R$ and Ω, the toroidal rotation frequency, are true flux surface functions, whereas γ_E as written is not. We see that RB_θ/B is much larger on the outboard midplane (particularly at large Shafranov shift α), where the ballooning mode turbulence lives. This would suggest that contrary to the our simple circular model, very much larger outboard shear rates may be operative.

III. TUNING AND VERIFICATION OF THE MODEL

We collect all the tuning parameters for the model here: $\hat{\alpha}=\frac{1}{2}$, $\hat{\beta}=0$, $\theta_{\rm rms}=\pi/3[1+0.2(q/2-1)]^{-1}[1+0.1(s-1)^2]^{-1/2}$, $\hat{k}=0.7$, $\hat{e}=0.9$, $\hat{b}=0.7$, $\alpha_p=0.5$, $N=10$, $k_m=0.02$, $k_M=0.5$. The overall transport strength parameter is $C=100$. Since we are tuning to the theory and not fitting to the experiment, the number of tuning parameters (be it 10 or 100) is not relevant. The present parameters were chosen for convenience and hand varied to produce the best overall ''best fit by eye'' to linear gyrokinetic stability and gyrofluid simulations, as demonstrated in the following figures. The procedure is only loosely systematic and not unique; the reader is left to judge the quality of the result from the figures.

The drift ballooning mode stability for a pure plasma depends on the $\hat{s}$, α, q, R/a, r/a, β_e, T_i/T_e, gradient lengths a/L_{n_e}, a/L_{n_i}, a/L_{T_e}, a/L_{T_i} the collisionality $\nu_{ei}/(c_s/a)$, and parallel velocity shear rate $\gamma_P=dV_\parallel/dr/(c_s/a)$. To illustrate how well the reduced GLF model reproduces the growths of the GKS code, we show scans around a standard tuning point at low collisionality ($\nu_{ei}=0$), and very high collisionality ($\nu_{ei}=\infty$), where the electrons become adiabatic (effectively $\sqrt{\epsilon}\to 0$ turning off the resistive modes). *Unless stated otherwise, the standard parameters throughout the paper are* $\hat{s}=1$, $\alpha=0$, $q=2$, $R/a=3$, $r/a=\frac{1}{2}$, $\beta=0$, $T_i/T_e=1$, $a/L_{n_e}=1$, $a/L_{n_i}=1$, $a/L_{T_e}=3$, $a/L_{T_i}=3$, $\upsilon_{ei}=0$, and $\gamma_P=0$, $k_y=0.3$. Figures 1 and 2 (3 and 4) show the low collisionality end (the adiabatic electron end) with the reduced GLF model in the left panels and the GKS growth rates to the right. Figure 1 (3) illustrates the somewhat higher growth rate with higher q, much decreased growth at larger $|\hat{s}|$ with less instability at negative $\hat{s}$, particularly for larger α. [Roughly, there is in an invariance with $\hat{s}-\alpha$ since $(\hat{s}-\alpha\sin\theta/\theta)\approx(\hat{s}-\alpha)$ is the combination entering the equation near the unstable ballooning point $\theta=0$.] Figure 2 (4) shows the increasing growth rate spec-

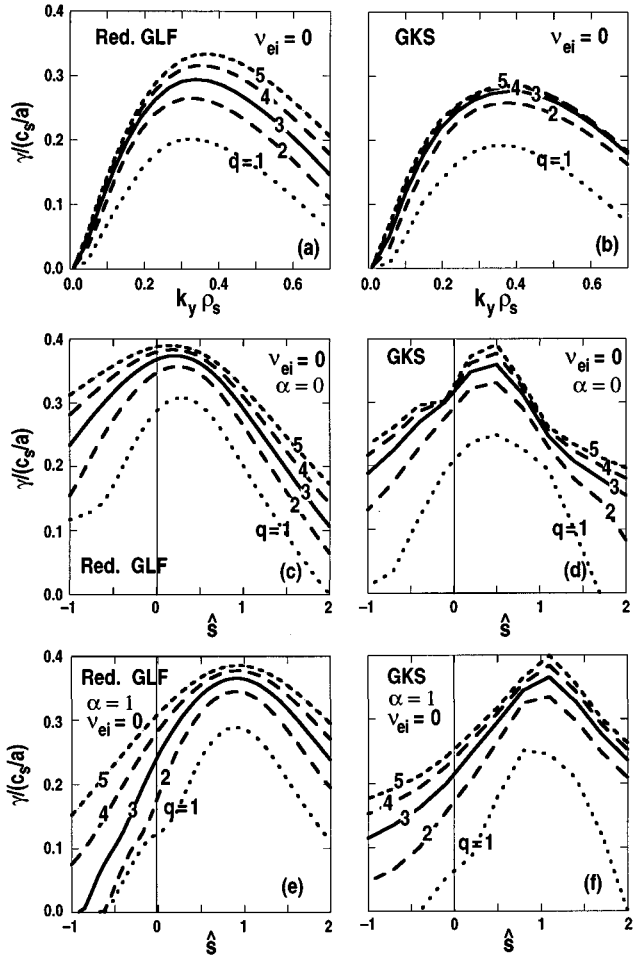

FIG. 1. Growth rate versus wave number (a), (b), versus shear at $\alpha=0$ (c), (d); versus shear at $\alpha=1$ (e), (f); and at various q in the collisionless limit. The reduced GLF model (left panels) and GKS code (right panels).

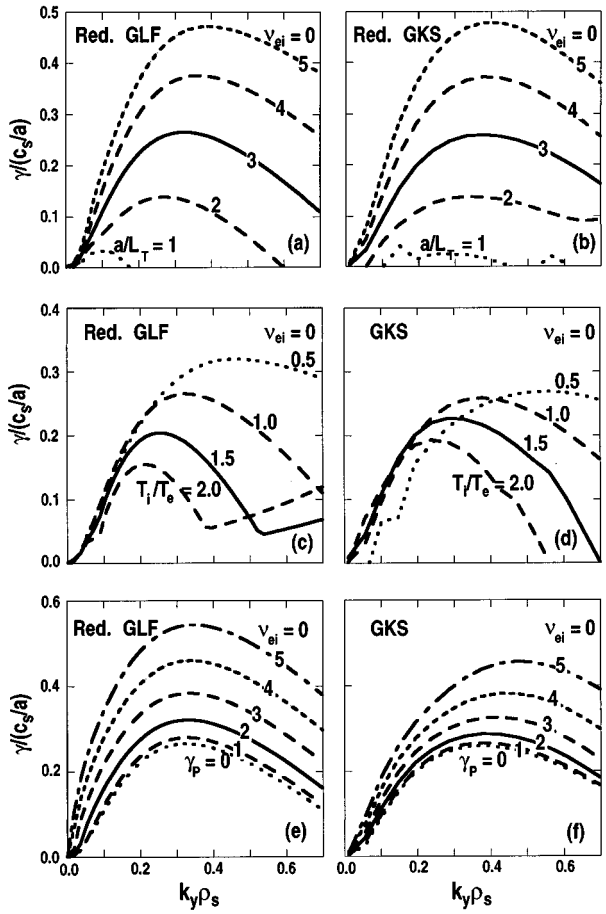

FIG. 2. The growth rate versus wave number at various temperature gradients (a), (b); ion to electron temperature ratios (c), (d); and parallel velocity shear rates (e), (f) in the collisionless limit. The reduced GLF model (left panels) and GKS code (right panels).

trum with increasing temperature gradient ($a/L_{T_e}=a/L_{T_i}$) at $a/L_{n_e}=a/L_{n_i}=1$ in Figs. 2(a) and 2(b), the decreasing growth rates with hotter ions in Figs. 2(c) and 2(d), and increased instability from parallel shear velocity (γ_P) in Figs. 2(e) and 2(f).

Again with the reduced GLF model to the left and GKS code to the right, Figs. 5(a) and 5(b) show how the ITG threshold at the adiabatic electron end ($\nu_{ei}=\infty$ dashed lines) is lost at the low collisionality end ($\nu_{ei}=0$ solid lines) if the density gradient gets large enough. There is actually a switchover from the ITG mode to the trapped electron mode branch (and a change in the sign of the real frequency) at low-temperature gradient and higher-density gradient. This is not apparent from plotting only the maximum growth rate. Figures 5(c) and 5(d) show how well the onset of the ideal MHD critical β is reproduced at $\beta_e=0.5\%$ [or $\beta=1.2\%$, consistent with the simple circular formula $(L_P/R)\hat{s}/q^2=1\%$]. Also note that the effect of finite β is rather weak or slightly stabilizing until the critical β is reached. The finite-β effects should give a small increase in confinement as most discharges are at less than half the critical β. However, because of the strong plasma shaping effects on the critical β, we cannot model the approach to the critical β accurately with our simplified geometry. Thus, in practice, we have generally used the model in the electrostatic limit with β set to 0. Finally Figs. 5(e) and 5(f) show the growth rate at the standard point versus collision frequency for the reduced GLF model and the GKS code. It is apparent from this figure, and also on close inspection of Figs. 1–4, that the fits are a little better at low collisionality than at high. Overall, we characterize the fits as generally good, but there is room for improvement.

To illustrate the tuning and basic properties of the transport coefficients for the model, Fig. 6 shows the q and $\hat{s}$ dependence of the model in the adiabatic electron limit. Figure 6(a) shows the strongly increasing q dependence of χ^i_{eff} [much stronger than for the growth rates in Figs. 3(a) and 3(b)]. This arises from the downshift of the spectral weight to low k_y, as shown in Fig. 6(b). This downshift is seen in the simulations.[3] In fact, we have used a spectrum of modes because it is difficult to obtain the strong q dependence of transport with a single k_y mode unless the single representative k_y is scaled inverse to q. Figure 6(c) shows the strong reduction of χ^i_{eff} with shear $\hat{s}$. The norm point for the model is taken from Beer's six-moment GLF 4π θ-box adiabatic electron ITG simulations at the standard point, save $q=1.5$ (instead of 2), $\chi^i_{\text{eff}}=8.5$.[4] This norm point is shown by the

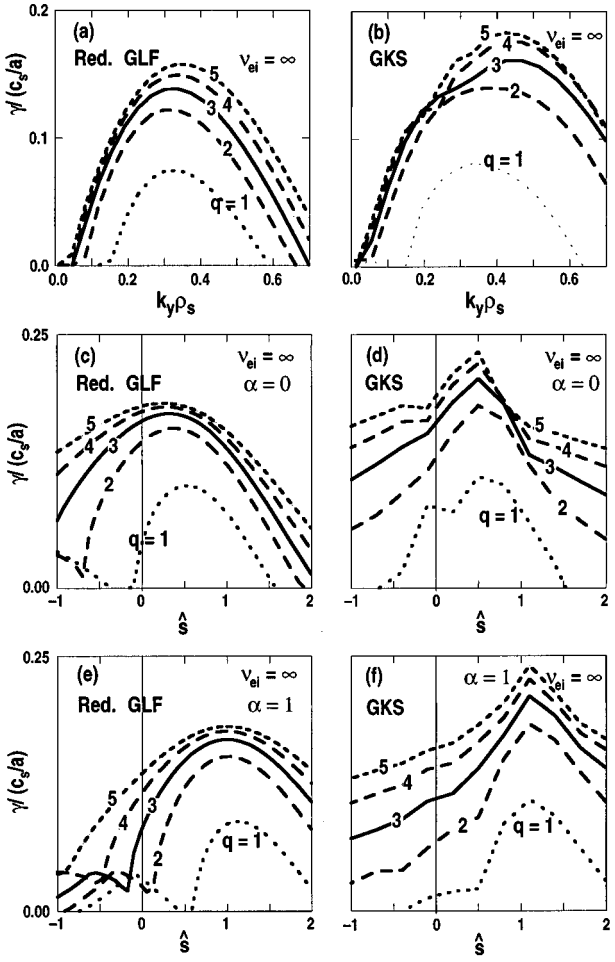

FIG. 3. The growth rate versus wave number (a), (b); versus shear at $\alpha = 0$ (c), (d); versus shear at $\alpha = 1$ (e), (f) at various q in the collisional (adiabatic electron) limit. The reduced GLF model (left panels) and GKS code (right panels).

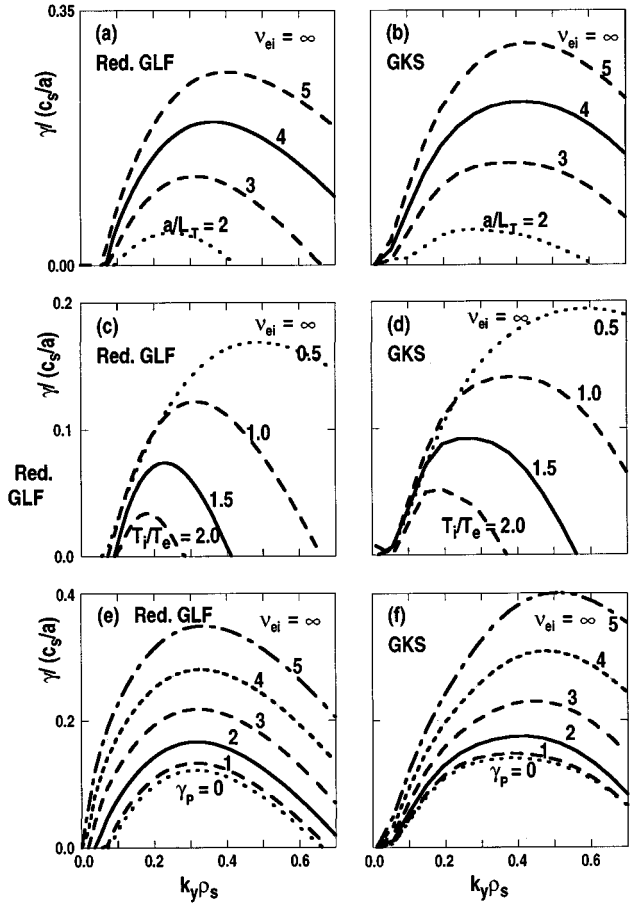

FIG. 4. The growth rate versus wave number at various temperatures gradients (a), (b); ion to electron temperature ratios (c), (d); and parallel velocity shear rates (e), (f) in the collisional (adiabatic electron) limit. The reduced GLF model (left panels) and GKS code (right panels).

hollow dot in Figs. 6(a) and 6(c). The results (W) of the four-moment GLF $2\pi\ \theta$ box from Waltz *et al.*,[2] renormed upward 6.4-fold to agree with the model at $q=2$, and $\hat{s}=1$ are shown with the solid dots and thin line. Note that the simulations show finite and continuous transport through $\hat{s}=0$ with less transport to $\hat{s}<0$, as does the model. The reverse shear effect is larger with increasing α [as with the growth rate in Figs. 3(e) and 3(f)] with the maximum in $\hat{s}$ shifted to the right roughly by α. The IFS-PPPL model[6] in the adiabatic electron limit is shown in Figs. 6(a) and 6(c) with X points on thin lines. There is close agreement between the models from moderate to high shear. The IFS-PPPL model did not attempt to account for the behavior of low and reverse shear. The reduced GLF model better represents the shear behavior but less well at the higher q behavior. Here $\hat{\beta}=0$ produces a ratio of 1.17 between the maximum near $\hat{s}=0.5$ and at $\hat{s}=1.0$ (at $q=2$), whereas $\hat{\beta}=1$ gives the steeper ratio 2.1 between the maximum at $\hat{s}=0.25$ and $\hat{s}=1.0$. (We note that a preliminary version of this model, with $\hat{\beta}=1$, had too steep of a falloff from low to high shear and a 2.3-fold smaller diffusion near the norm point. The present model is closer in agreement to the IFS-PPPL model near the norm point.)

Figure 7 shows the behavior with temperature gradient in comparison to the IFS-PPPL model[6] and to the renormed Waltz *et al.*,[2] simulations (W). The latter simulations do indeed show the saturation with temperature gradient captured better by the IFS-PPPL model. The reduced GLF model can get this behavior with $\hat{\alpha}$ closer to $\frac{1}{4}$, but then the linear decrease of diffusion with γ_E seen in the simulations is not captured. Since the application the models tend to stay near marginality, we have chosen to represent the weak gradient end. (Note that the four-moment GLF simulations[2] miss the correct GKS threshold at $a/L_T=1.3$, getting instead 1.8.)

Figure 8(a) shows the almost linear decrease of χ^i_{eff} with γ_E to the point of stability at $\gamma_E=\gamma_{\max}$ at both high and low collisionality. Figure 8(b) illustrates how the spectrum shifts to higher k_y as the $E\times B$ rotational stability point is approached. Figure 8(b) [as well as Fig. 6(b)] illustrate a weakness of the model and how the weight of every representative k_y in the spectrum is determined by its own stability. While the upshift in spectrum with γ_E (and the downshift with q) are to be expected trends of nonlinear simulations, nonlinear interactions prevent any portion of the spectrum to be completely depopulated because of stability.

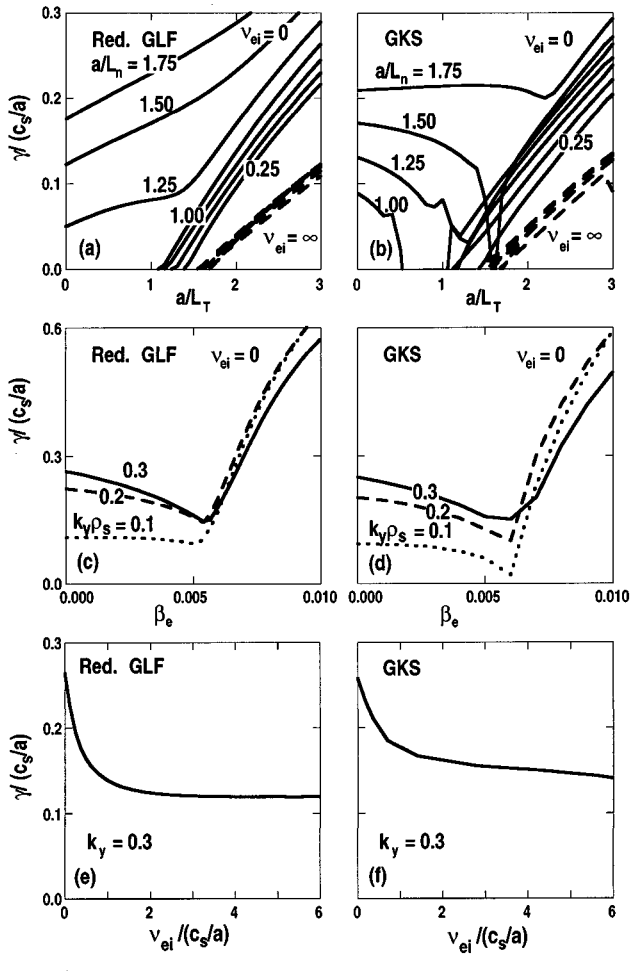

FIG. 5. The growth rate versus the temperature gradient at various density gradients (a), (b); versus beta at low wave numbers (c), (d); versus collisionality (e), (f) in the collisionless limit. The reduced GLF model (left panels) and GKS code (right panels).

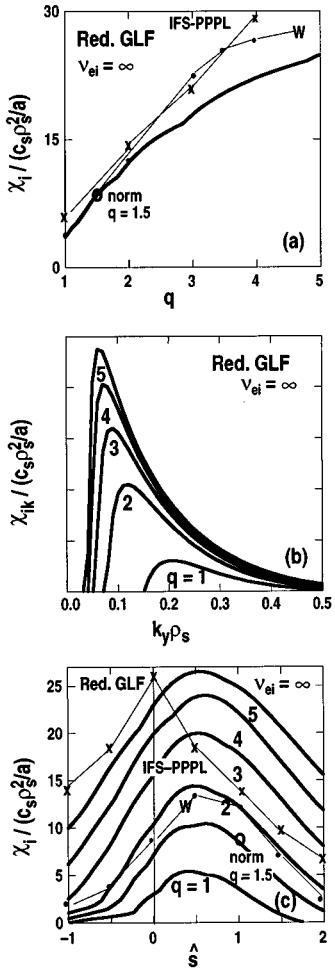

FIG. 6. Ion energy diffusivity versus q (a). The wave number spectrum of ion energy diffusivity at various q (b) Ion energy diffusivity versus shear at various q (c). The collisional (adiabatic electron) limit. The IFS-PPPL model and renormed Waltz *et al.*, simulations (W) shown at $q=2$ in (c).

Finally, Fig. 9 shows the dependence on collisionality for χ^i_{eff} and χ^e_{eff} from the model (solid lines) in comparison to Beer's four-moment low resolution simulations[4] renormed upward by 2.3-fold (dashed lines) to bring them in line with the six-moment high resolution adiabatic electron ITG case at extreme collisionality. No free parameters are left to change the fit.

IV. ρ^* DEPENDENCE OF TRANSPORT BIFURCATIONS OF THE MODEL

Turbulent transport fluxes typically increase with their corresponding plasma gradients in density, temperature, or rotation at low values; but in some instances, they can decrease at high gradients, allowing the transport to bifurcate at a critical flux level jumping to a state of enhanced confinement: a higher gradient supported by the same flux. Our comprehensive model contains transport bifurcation mechanisms based on rotational shear stabilization and possibly on α stabilization. In this paper, we discuss only the former, which we believe is most relevant to DIII-D NCS core confinement treated in Sec. V. Figure 10 illustrates some special idealized limits in which the turbulent transport fluxes are plotted against driving gradients and show a maximum in the flow. Figure 10(a) is a heat flow bifurcation and Fig. 10(b) a momentum flow bifurcation. Arbitrary amounts of neoclassical fluxes, which increase linearly with gradients, have been added as indicated. In the case where there is no toroidal rotation, the $E\times B$ rotation is in balance with the diamagnetic rotation and the neoclassical poloidal rotation. In the

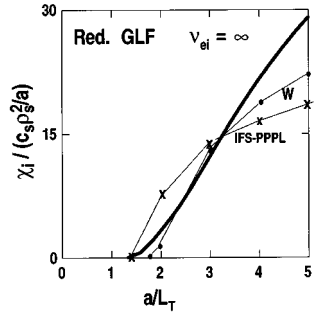

FIG. 7. Ion energy diffusivity versus temperature gradient at various density gradients in the collisional (adiabatic electron) limit in comparison to the IFS-PPPL model and renormed Waltz *et al.* simulations (W).

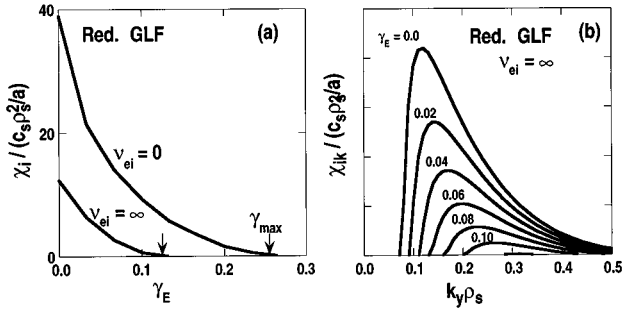

FIG. 8. Ion energy diffusivity versus the $E\times B$ rotational shear rate in collisional and collisionless limits (a). The wave number spectrum of ion energy diffusivity at various $E\times B$ rotational shear rates in the collisional (adiabatic electron) limit.

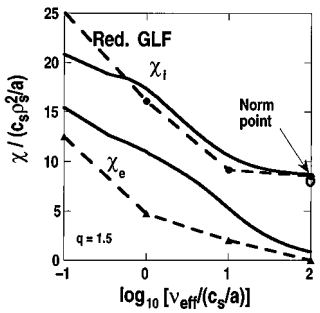

FIG. 9. Ion and electron energy diffusivity (model solid lines) versus collisionality in comparison to high resolution simulations by Beer, *et al.* (dashed lines). (Resistive modes at high collisionality is not included.)

banana regime, this is approximately the same as $E\times B$ in balance with a density gradient diamagnetic rotation [see Eq. (16a) with $\alpha_{1\text{neo}}\approx 0$]. Ignoring second derivatives of the density gradient, the $E\times B$ rotational shear has a leading term proportional to the temperature gradient that drives the energy flow: $\gamma_E=(\rho^*\cdot a/L_n)(a/L_T)+\cdots$. Figure 10(a) shows how quickly the power flux $(\hat{Q})$ (normed to $nTc_s\rho^{*2}$) threshold (maximum versus gradient) for this bifurcation increases with decreasing density gradient and, more importantly, with decreasing relative gyroradius ρ^*. In this particular instance, the power threshold P_{th} has much worse than Bohm-like $a^2nTc_s\rho^*$, or approximately $P_{\text{th}}/(a^2nTc_s)\propto(1/\rho^*)^{1/2}$. This type of diamagnetic rotational stabilization heat flow bifurcation has been proposed as a mechanism for the L/H transition.[16] The unfortunate scaling to lower ρ^* may be why the H-mode power threshold has such poor scaling toward reactors at smaller ρ^*. A second rotational shear mechanism can result from $E\times B$ rotation arising from beam-driven toroidal rotation. Shear in the toroidal rotation γ_P drives instability and transport, but for purely toroidal rotation (ignoring smaller diamagnetic components) $\gamma_E=(r/Rq)\gamma_P$ and the $E\times B$ stabilization can win out (particularly at low q/r). Figure 10(b) shows how the normed toroidal momentum flux or viscous stress $(\hat{\Pi})$ can bifurcate to a state of larger rotational shear at a fixed temperature gradient. Note that at high values of q/r, the high gradient-enhanced rotation state can still be turbulent because of γ_P drive. This type of momentum bifurcation has been proposed as the cause of the Very High- (VH-) mode-enhanced confinement in DIII-D,[17] and we argue in Sec. V that is dominant in the DIII-D NCS core transport barrier. The mechanism has been seen in ITG turbulence simulation of rotationally stabilized viscosity.[2] Since not only the viscosity η_ϕ but also the heat diffusivity χ will be smaller in the enhanced rotational state, and in steady state the heat and momentum flow maintain a constant ratio, the temperature gradient will also jump to a higher value. In reality, the bifurcations involve transport in density, temperature, and rotation, and several mechanisms may contribute simultaneously. The multichannel nature of the L/H mode, the VH mode, and internal transport barrier bifurcation have been treated by Staebler *et al.*,[17] with rotational stabilization of heuristic models. Our purpose here is to quantify these bifurcations with a comprehensive physical transport model. Figure 10(c) shows a more comprehensive test of a multichannel bifurcation, where we have plotted contours of the momentum flux and the power flux against both the rotational shear γ_P and temperature gradient (a/L_T). Since here $\gamma_E=(r/Rq)\gamma_P-(\rho^*\cdot a/L_n)(a/L_T)$, both diamagnetic heat flow bifurcations and toroidal momentum bifurcations types are indicated. The three-point intersection of $\hat{\Pi}$ and $\hat{Q}$ contours illustrate true bifurcation: b1, u1, n1 are (respectively) the bifurcation, unstable, and neoclassical points for the diamagnetic type and b2, u2, n2 are the corresponding points for the toroidal rotation type bifurcations.

Staebler *et al.*,[18] have recently suggested a simple interpretation of the bifurcation conditions for this model. Basically, one can be assured that the profile passes through a transport bifurcation with a critical power and flow threshold if $d\gamma_{\text{net}}(\rho)/d\gamma_E(\rho)\leqslant 0$. This is the appropriate generalization of the $d\hat{Q}/d(a/L_T)\leqslant 0$ and the $d\hat{\Pi}/d\gamma_P\leqslant 0$ transport

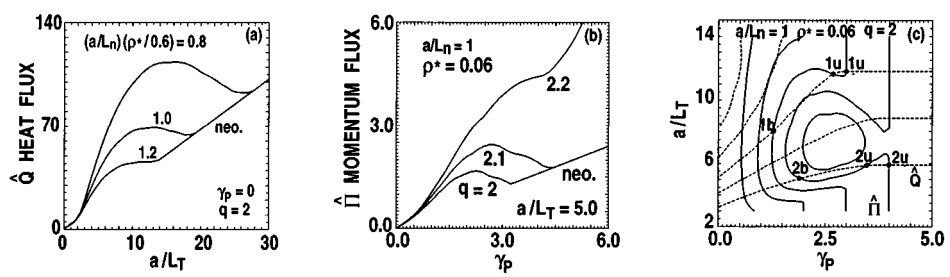

FIG. 10. Bifurcations: diamagnetic heat flow (a), toroidal momentum flow (b), and combined mechanisms (c) showing intersecting contours of $\hat{Q}$ and $\hat{\pi}$.

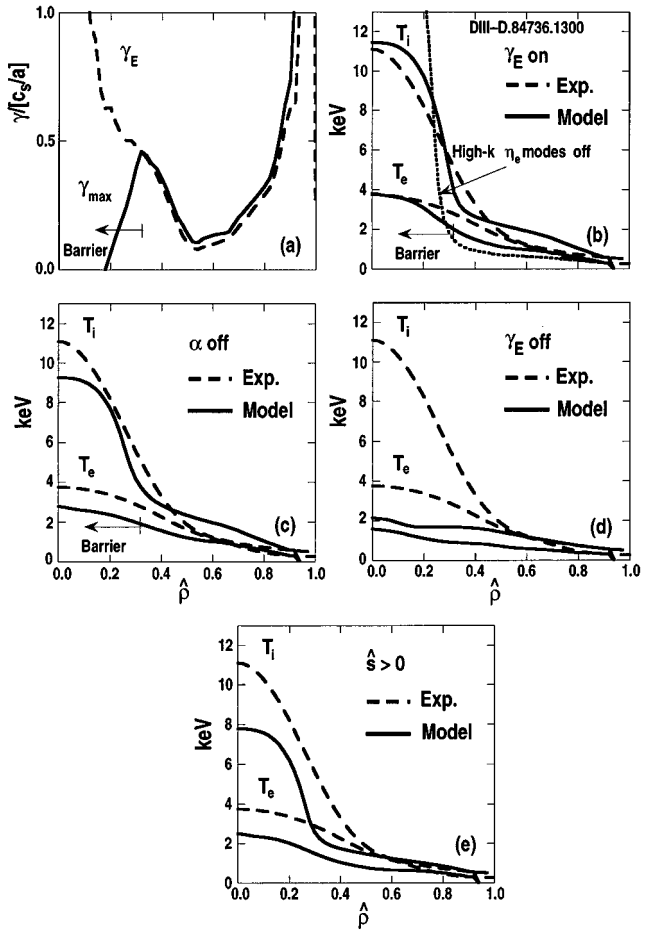

FIG. 11. Radial profile s of the maximum mode growth rate in comparison to the $E\times B$ shear rate (a) and the model (solid lines) and experimental (dashed lines) temperatures (b) from a transport code simulation of the NCS DIII-D discharge 84736 at 1300 ms. The effect of individually turning off α stabilization is shown in (c), negative shear in (d), and $E\times B$ rotational shear in (e).

unstable regions in Figs. 10(a) and 10(b). It can be applied as a test to any given instantaneous growth rate profile. We illustrate this in our first application of the model in the next section.

V. ROTATIONAL SHEAR TRANSPORT BARRIER IN DIII-D NCS DISCHARGES

A distinguishing feature of the present model is its ability to describe many aspects of enhanced core confinement such as the NCS DIII-D discharges[9] without special modification. Taking the rotational shear rates from the experiment, we find that γ_E can become so large as to exceed $\gamma_{\max}$ and shut off transport from low-k drift ballooning modes in all channels allowing only neoclassical transport and higher-k η_e-mode transport over a large core plasma. Taking a DIII-D NCS discharge (shot 84736 at 1300 ms),[9] Fig. 11(a) shows the profile of γ_E [determined from the experimental temperature, density, and rotational profiles using Eqs. (15) and (16)] in comparison to the profile of the model maximum growth rate $\gamma_{\max}$, consistent with the model temperature profiles shown in Fig. 11(b). It is clear that the condition $d\gamma_{\rm net}(\rho)/d\gamma_E(\rho)\leqslant 0$ is well satisfied in the core region. The agreement between the model temperature profiles and the experiment is an example of good agreement for the model. While the energy flow ion channel is neoclassical in the core where $\gamma_E > \gamma_{\max}$, the electron channel is not neoclassical, because the model has included the electron transport from the high k_y η_e modes. Their $(m_i/m_e)^{1/2}$ larger growth rates prevent them from being stabilized by γ_E. Normally, their transport is so small as to be ignorable, but inside the ion neoclassical transport barrier they prevent the electron temperature from running away with neoclassical electrons. The thin line in Fig. 11(b) shows the electron neoclassical runaway obtained if the η_e modes are not included. A 25% decrease in the experimental γ_E profile results in a peak ion temperature drop of more than 50%. Although for numerical reasons, we have not yet succeeded in reproducing the formation of this core transport barrier with a full-time-dependent simulation of the heat and toroidal momentum channels and determining the scaling of power thresholds with ρ^*, there seems little doubt that it must be dominated by a momentum channel bifurcation. Here γ_E is about 150% cotoroidal rotation with a compensating 50% diamagnetic component at the barrier ($\hat{\rho}=0.3$). The maximum negative shear is $\hat{s}=-0.25$ and shear reversal point is near $\hat{\rho}=0.4$. The maximum α is 0.7 in the barrier. Figure 11(c) shows the effect of setting $\alpha=0$ and Fig. 11(d) the effect of setting $\gamma_E=0$. While some effect of α stabilization in producing better core confinement is evident, no barrier at all is evident without rotational stabilization from γ_E. Figure 11(e), which replaces the experimental q profile with a similar but monotonic one and removes the reverse shear, shows that while the negative shear prevents core ideal MHD ballooning modes, the improved transport with reversed shear [comparing Fig. 11(b) to 11(e)] is not the dominant cause of the barrier. In this particular NCS discharge, there is no significant improvement experimentally in the core plasma transport (no large density peaking), and although core toroidal momentum diffusivity (viscosity) is significantly reduced, it may not reach neoclassical levels (as does the ion heat transport). This is in contradiction to our model as formulated. We can only speculate that had we allowed high-k η_e modes to have some nonadiabatic ion response; or, more likely, allowed some of the high-k η_e mode turbulence to cascade to lower k_y, where the ions could respond, then some level of turbulent plasma diffusion and viscosity might survive. In fact, a general weakness of our model is that it counts no transport for stable k_y modes as we noted at the end of Sec. III.

VI. TESTING AGAINST THE ITER TRANSPORT PROFILE DATABASE

Using our fast ''shooting'' transport code,[7] the model has been tested against datasets from the ITER transport database[11] of more than 50 discharges from the DIII-D, Joint European Tokamak (JET),[19] Tokamak Fusion Test Reactor (TFTR),[20] and other tokamaks. Table I shows a selected set of some 29 of H- and L-mode discharges (no Supershots) used to test numerous models in Ref. 11. (The number of shots actually tested is given in the table.) We use experimental boundary conditions at the 90% toroidal flux radius,

TABLE I. Testing against the ITER transport profile database.

Model	Number	$R\tau$	$\Delta R\ \tau$	$R\tau_b$	$\Delta R\ \tau_b$	$RnT\tau$	$\Delta R\ nT\tau$
IFS-PPPL	27	0.86	0.22	0.79	0.33	0.70	0.41
GLF	28	0.95	0.22	0.95	0.33	0.98	0.47
RW_e	$\Delta R\ W_e$	RW_i	$\Delta R\ W_i$	RW_{eb}	$\Delta R\ W_{eb}$	RW_{ib}	$\Delta R\ W_{ib}$
0.88	0.22	0.86	0.23	0.81	0.37	0.79	0.33
0.95	0.22	0.97	0.25	0.95	0.35	0.98	0.38

and take density, current profiles, and rotational rates [γ_E using Eqs. (15) and (16)] from the experiment. The power deposition profiles are taken from the experiment, with the exception of the electron–ion transfer. We then test the model by comparing the ratios of model to experimental confinement times ($R\tau$) or stored energy. A rms deviation ($\Delta R\tau$) from perfect ($R\tau=1$) of 22% is found. A rms deviation in $n_0T_0\tau$ values ($\Delta R\ nT\tau$) of 47% is obtained. One might hope for 10% in $\Delta R\ \tau$ (or 20% in $\Delta R\ nT\tau$) as a correlation in the range of experimental error bars, but uniform testing of several currently popular empirical and theory based models on this dataset have not found significantly higher correlation.[7] The table shows a comparison of the model with the IFS-PPPL model. The scatter (particularly in $\Delta R\ nT\tau$) is better for the IFS-PPPL model,[6] but the overall averages ($R\tau$ and $RnT\tau$) are closer to unity in the present model. It should be noted that neither of these critical gradient models can be easily adjusted by an overall multiplier on the diffusivities. In fact, reducing the overall diffusivity by a factor of $\frac{1}{2}$ makes almost no change in the table, indicating that the general operation of both models is near the marginal point. The rms deviation in ''incremental stored energy'' (or energy stored above the boundary pedestal temperature) that we label $\Delta R\ \tau_b$ is 33%. This measure discounts the forced agreement with the boundary temperatures taken from the experiment. Figure 12 gives a graphic illustration of the stored energy ratios for the present reduced GLF model in Fig. 12(a), the IFS-PPPL model in Fig. 12(b), and the GSLs in Fig. 12(c). (We used ITER89P[21] for the L modes and ITER93H[22] for the H modes.) The $R\tau=1.01$ and $\Delta R\ \tau=30\%$ for the GSLs. If we regard labeling the mode by ''L'' or ''H'' as information from the boundary, then the theory-based models with $\Delta R\ \tau$ at 22% are outperforming the empirical GSLs on this restricted dataset. (Note that the GSLs typically have $\Delta R\ \tau$ in the range of 11%–12% using the order of 500–1000 discharges). Even comparing the models with $\Delta R\ \tau_b=33\%$ and the GSLs with $\Delta R\ \tau=30\%$, then the models are at least competitive with GSLs. The latter statement discounts the ability of transport models, like the reduced GLF model, to describe enhanced core confinement discharges without resorting to *ad hoc* variables.

The IFS-PPPL significantly underpredicts the average data in part because it did not include rotational stabilization. Table II shows the statistical effect of leaving out the $E\times B$ rotational stabilization in the present model. In comparison with Table I, a general reduction of about 13% average confinement time is apparent. (We hasten to note that this dataset does not include shots with core transport barriers for which rotational stabilization appears to be essential.) Table II also shows the destabilizing effect of turning off the impurity dilution (about 7% in average confinement time). Curiously, the entry without dilution shows a better scatter in $\Delta R\ nT\tau$ than with dilution. This could indicate a better model for the impurity dynamics beyond simple dilution or more consistent data is needed. For completeness, the last entry in Table II shows the effect of finite β is overall to stabilize and raise the confinement time considerably. Rather, poorer results are obtained. Recall that the finite β of the model is likely very unreliable because the effect of finite β must be with respect to the MHD β limit, which cannot be reliably obtained without real geometry.

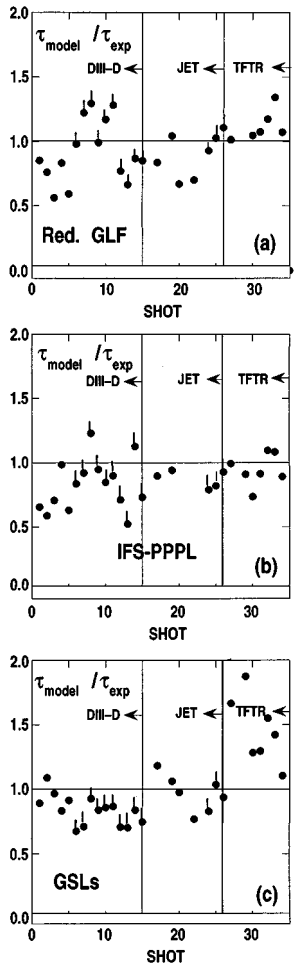

FIG. 12. The ratio of the model to experimental confinement times (or total stored energy) for the reduced GLF model in (a), the IFS-PPPL model in (b), and the standard GSL ITER89P and ITER93H in (c). A selected set of L modes (dots) and H modes (flagged dots) from the ITER transport profile database.

TABLE II. The effect of modifications on the model to be compared with the results in Table I.

Model	Number	$R\tau$	$\Delta R\ \tau$	$R\tau_b$	$\Delta R\ \tau_b$	$RnT\tau$	$\Delta R\ nT\tau$
GLF no γ_E	27	0.82	0.26	0.74	0.39	0.77	0.47
GLF no dil	26	0.88	0.23	0.83	0.33	0.82	0.42
GLF fin β	26	1.07	0.27	1.15	0.44	1.25	0.61

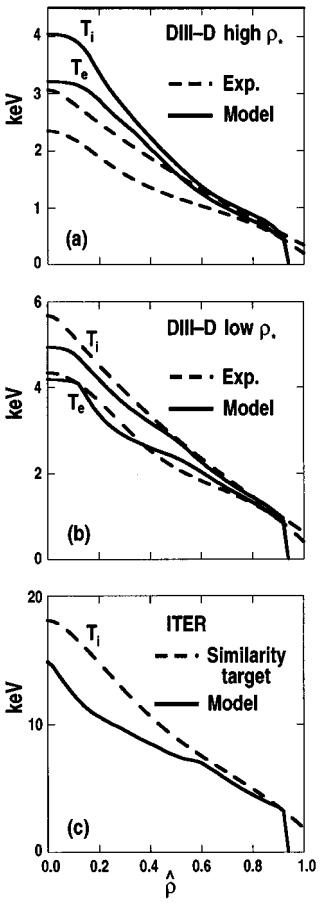

FIG. 13. Profiles of the model (solid lines) and experimental (dashed lines) from high-r^* (a) and low-r^* (b) DIII-D ITER demonstration discharges. The model projection to the ITER discharge at scaled magnetic field, size, and density shown in (c) with projected temperature (solid line) and similarity target temperature (dashed line).

VII. ITER IGNITION PROJECTIONS FROM DIII-D DIMENSIONALLY SIMILAR DISCHARGES

It is generally believed that the most reliable way to project to ITER is to vary only the ρ^* parameter. The dependence on ρ^* has special significance,[23] since it is the only dimensionless parameter, which, in principle, cannot be matched in extrapolating to reactors. Figure 4 illustrates the transport code simulations of the DIII-D ITER H-mode demonstration dimensionally similar ρ^*-scaling discharges: a high-ρ^* shot (shot 82788 with $B=0.95T$) in Fig. 13(a) and a low-ρ^* shot ($1.6\times$ lower ρ^*) (shot 82205 with $B=1.89T$) in Fig. 13(b), with the rotational effects turned on. This pair was found experimentally to have gyro-Bohm global confinement time or power scaling.[12] The toroidal field B_T is doubled from $0.9T$ to $1.8T$, with maximum transport power flow (at 90%) almost exactly doubling from 2.4 to 4.8 MW. As we will demonstrate, however, the rotational stabilization is an important consideration for these discharges. In fact, it is difficult (if not impossible) to keep the same Mach number (V_ϕ/c_s) fixed as it should be for ''dimensionally similar discharges'' [23] with the same β, collisionality, safety factor, shape, and allowing only ρ^* to change. It could be argued that dimensionally similar discharges should be *defined* with the Mach number proportional to ρ^*. For these shots the peak Mach number, in fact, increases from about 0.14 to 0.26, going to smaller ρ^*. Rotational effects are complicated and counteracting: diamagnetic against toroidal corotation in determining γ_E, and destabilization by γ_P against stabilization by γ_E. Ignoring rotational effects (setting $\gamma_E=0$ and $\gamma_P=0$), and turning our model into a gyro-Bohm scaling model, drops the peak temperatures by about 22% in the high-ρ^* discharge [$T(0)$ from 3.6 to 2.8 keV with the experimental value at 2.7 keV] and by 15% in the low-ρ^* discharge [$T(0)$ from 4.6 to 4.0 keV with the experimental value at 5.0 keV]. [Here $T(0)$ is the $e-i$ average central temperature.] Thus, rotation affects both discharges about equally according to the model. The model is very close to marginality since a $0.5\times$ reduction in the model diffusivity strength makes virtually no difference in the predicted temperatures.

The fits to these discharges are typical of the model and deserve a detailed discussion, particularly in relation to ρ^* scaling. The fit to the low ρ^* is quite good and the fit to the high ρ^* is rather poor. Taking the low ρ^* as the reference discharge, the model predicts a higher temperature at high ρ^*, suggesting that the model has a deviation from gyro-Bohm scaling in the direction of Bohm transport: $T(0)=3.5$ keV compared to the experimental 2.7 keV [see Figs. 4(a) and 4(b)]. However this is misleading, if one considers the imperfections in the experimental similarity conditions. Projecting by $B_T^{2/3}$ for perfect similarity from the low-ρ^*, the high-ρ^* discharge should have had an experimental value of $T(0)=3.2$ keV, i.e., the actual discharge at 2.7 keV had a 16% lower temperature than perfect similarity requires. Thus, the model is behaving almost gyro-Bohm-like, even with the rotational effects. The discharges had good β similarity but poorer similarity in collisionality. The high-ρ^* shot, in fact, has a dissimilar density profile with about 20% larger density than a perfect $B_T^{4/3}$ projection from the low-ρ^* discharge and, more importantly, a 35% smaller logarithmic density gradient. The lower-density gradient will tend to turn off the trapped electron drive. The model is, in fact, very sensitive to density gradients as the trapped electron modes onset with increasingly peaked density profiles. For example, if in the high-ρ^* discharges we use the density profiles projected by perfect $B_T^{4/3}$, similarity from the low-ρ^*, then the model average peak temperature falls from 3.5 to 3.0 keV, which is closer to the 2.7 keV experimental value. A further proof of the model sensitivity to density profiles is demonstrated by noting that we, in fact, treated the low-ρ^* case by solving for the density profile consistent with the experimental plasma flow over the inner 60% of the plasmas. This leads to a density profile that is almost imperceptibly different from the given experimental profiles, yet the self-consistent density profile gives a much better fit to the temperature data than using the experimental density profile. Thus, it is difficult to be sure that the rather poor fit for the low-ρ^* discharge may, in fact, be within the experimental error bars given the uncertainty in the experimental density profiles. (The high ρ^* is less sensitive to the density profile and solving for the density profiles as in the low-ρ^* case makes little difference.) Furthermore, it is very difficult to sort out experimentally how much the rotational effects

break the otherwise gyro-Bohm scaling of the model in the context of imperfect similarity conditions, i.e., imperfect density gradient similarity can have a bigger effect on the model than the effect of rotational shear breaking the gyro-Bohm scaling.

It is well to keep in mind when comparing gyro-Bohm scaling to Bohm scaling the large difference in power scaling (which has a small experimental error) and the smaller difference in temperature (which may have a significant experimental error). For example, in going from low to high ρ^* by changing the magnetic field $2\times$, the power to maintain perfect similarity is $2\times$ smaller for gyro-Bohm scaling and $3.17\times$ smaller for Bohm scaling. However, a Bohm model normed to the low-ρ^* discharge in a perfect gyro-Bohm scaling experiment would produce a temperature only 26% larger for the high-ρ^* discharge than a similarly normed gyro-Bohm model.

Figure 13(c) shows the model ignition simulation of the low-ρ^* discharge scaled up by $3.2\times$ in the B field and $4.6\times$ in the radii to ITER at a $7.8\times$ smaller ρ^*. The dimensionally similar peaked density profiles with 10% ion deficit is scaled by $2.9\times$ from $\overline{n_e}=5-15\times10^{13}$ cm^{-3} and the H-mode pedestal $e-i$ average temperature at 90% is scaled by $3.6\times$ from 0.95 to 3.5 keV. Ignoring toroidal rotation, this scaling keeps all dimensionless parameters fixed except ρ^* (see Ref. 23 for these scaling ratios). In fact, the ignited discharge can be assumed to have negligible toroidal rotation and insignificant diamagnetic rotation; thus, we assume $\gamma_E=0$, and $\gamma_P=0$ for the ITER target plasma. The temperature equilibrated ignited state is assumed to have auxiliary power beyond self-consistent alpha-power heating less bremsstrahlung (as well as synchrotron) loss. The model temperature self-consistent with the net heating falls short of the dimensionally similar target temperature profile. The similarity target with $3.6\times$ larger $e-i$ average DIII-D temperature profile is shown as a dashed line. If the diffusivity strength of the model is reduced by $0.5\times$, the self-consistent heating temperature is coincidentally close to the similarity target temperature. At $1\times$ (and $0.5\times$) the model diffusivity strength, the peak temperature is 14.5 (16) keV, the alpha power production is 222 (310) MW (the latter close to the ITER design point) and the transport loss (alpha power less radiation) through the boundary is 150 (230) MW. The nominal transport power to support the H-power threshold is 100–150 MW. In contrast to the DIII-D cases (and nearly all other existing experimental cases we have examined), the dependence on the diffusivity strength means that there is enough transport power from the alpha heating to drive the model above the ITG threshold. In the half-strength case ($0.5\times$diffusivity), which fits the DIII-D case as well as the full strength case but that is near the similarity target profile, it requires close to a $53\times$ Bohm-like scaling of the 4.8 MW transport power ($48\times$ to be precise) from the DIII-D discharge to 255 MW (or, to be precise, 230 MW), even though the gyro-Bohm scaling of the DIII-D shots at perfect similarity would require only 6.8×4.8 or 33 MW of transport power. This loss of gyro-Bohm scaling is due to forced equilibration that removes any hot ion stabilization and, more importantly, loss of rotational stabilization at lower ρ^* and negligible toroidal rotation. If we had retained the rotational shear rates fixed at DIII-D experimental values, i.e., γ_E and γ_P fixed in units of c_s/a or fixed Mach number that turns the model into a purely gyro-Bohm model projection, the peak temperatures would have been 21 (25) keV, and the alpha power driven up to 450 (590) MW, with transport power at 360 (490) MW. (The β limit would be exceeded in these cases.) Thus, a purely gyro-Bohm scaling from the DIII-D demonstration discharge implies an overdesign of ITER,[24] but according to the present model, the certain loss of rotational stabilization allows only nominal (or close to nominal) operation with the given boundary conditions and density profile. Coincidentally, at $1\times$ the model diffusivity, the IFS-PPPL model[6] gives almost identical results for this particular projection. However, we note that for the reduced GLF model, in contrast to the IFS-PPPL model, the alpha power production is less sensitive to flattening the density profile from the moderately peaked density case illustrated here. This results because the loss in alpha power production with density peakedness is compensated by the decrease in transport losses from the trapped branch that is not present in the IFS-PPPL model. For example, instead of using the moderately peaked density profiles we use perfectly flat density profiles corresponding to the $\rho=90\%$ boundary densities at $n_e=11.3\times10^{13}$ cm^{-3} and $n_i=10.5\times10^{13}$ cm^{-3}, the reduced GLF model (IFS-PPPL) model has a peak temperature of 21 keV (14 keV) with 210 MW (120 MW) of alpha power and 155 MW (70 MW) of transport power. In this flat density case, the reduced GLF model is considerably more optimistic than the IFS-PPPL model.

A key uncertainty in projection of the H modes to ignition is whether the pedestal temperatures can, in fact, be maintained at the rather high similarity values used (3.5 keV). Reference 25 argues a very pessimistic scaling of the H-mode pedestal pressure (or β) with ρ^* suggested by an edge diamagnetic shear layer (the width scaled by the poloidal gyroradius $\rho_{\rm pol}$) limited to MHD stability: $\beta q^2\approx\rho_{\rm pol}/R$. This scales to L-mode edge temperatures in ITER. Here make no attempt to assess the experimental trends in favor or possible counterexamples to this pedestal scaling. We only note that at 80% of the assumed pedestal temperature, the model predicts that ignition becomes marginal as $T(0)$ drops from 14.5 (16) to 11.8 (14.3) keV, the alpha power to 115 (172) MW, and the transport power to 60 (105) MW again referring to $1\times(0.5\times)$ model diffusivity strength. The latter is likely insufficient to support the H-mode threshold. Again, almost identical results are obtained from the IFS-PPPL model[6] in this moderately peaked density profile case.

VIII. DISCUSSION

In summary, our comprehensive dispersion theoretic transport model allows a more systematic extension of previous formula-based gyrofluid transport models such as the IFS-PPPL model. We have demonstrated the important effects of rotational shear stabilization (and α stabilization) in reverse shear or DIII-D NCS discharges and the importance of the loss of rotational shear stabilization and broken gyro-Bohm scaling in projecting dimensionally similar discharges

to ignition. The more comprehensive model, however, has not led to demonstratively better descriptions of core energy confinement for ordinary L- or H-mode discharges, apart from the effect of $E\times B$ rotational shear stabilization reducing the overall offset from the experimental database average confinement time. While the model gives transport coefficients for particle and momentum transport based on quasilinearity, neither self-consistent treatment of the these channels, nor dynamical solution of multichannel transport bifurcations were explored in this paper. There are several possibilities for improving the model agreement with experiment. One is to determine if more complete solutions with model consistent density profiles helps. We know that is the case in some instances, but it is technically difficult to treat the particle sources over the whole plasma. Another approach would be to abandon the approximate reduced gyrofluid equations entirely and use the accurate linear gyrokinetic code solutions directly. Indeed some effort has been made in this direction,[25] but these methods are still computationally very slow and not yet practical for treating many cases. Certainly, the direct use of a linear gyrokinetic code will allow a tractable approach to real geometry, whereas tuning the present reduced GLF model beyond the simple s-α equilibrium will become awkward. Both the reduced GLF approach and a direct gyrokinetic approach must rely on the use of quasilinear transport flow relations and mixing rate rules and neither can proceed faster than more and better documented nonlinear simulations will allow. An important caveat on these approaches, particularly for treating more than just the energy or temperature transport channels, is that quasilinearity and mixing rules are typically tested against simulations well above the marginal or critical temperature gradients (where good statistics can be obtained), yet the models in application tend to stay near marginality.

ACKNOWLEDGMENTS

This is a report of work sponsored by the U.S. Department of Energy under Grant No. DE-FG03-95ER54309 and Contracts No. DE-AC02-76CH03073 and No. W-7405-ENG-48. J.A.K. was supported by Niels Stensen Stickting and the National Organization for Scientific Research, and Euratom-FOM.

[1]M. Kotschenreuther, Bull. Am. Phys. Soc. **37**, 1432 (1992).
[2]R. E. Waltz, G. D. Kerbel, J. Milovich, and G. W. Hammet, Phys. Plasmas **2**, 2408 (1995); *ibid*. **1**, 2229 (1994).
[3]G. W. Hammett, M. A. Beer, J. C. Cumming, W. Dorland, W. W. Lee, H. E. Minick, S. E. Parke, R. A. Santoro, M. Artun, H. P. Furth, T. S. Hahm, G. Rewoldt, W. M. Tang, R. E. Waltz, G. D. Kerbel, and J. L. Milovich, *Plasma Physics and Controlled Nuclear Fusion Research* 1994 (International Atomic Energy Agency, Vienna, 1996), Vol. III, p. 273.
[4]M. A. Beer, G. W. Hammett, G. Rewoldt, E. J. Synakowski, M. C. Zarnstorff, and W. Dorland, Phys. Plasmas **4**, 1792 (1997); also see M. A. Beer and G. W. Hammett, Phys. Plasmas **3**, 4018 (1996); M. A. Beer and G. W. Hammett, *ibid*. **3**, 4046 (1996); M. A. Beer, ''Gyrofluid models of turbulent transport in tokamaks,'' Ph.D. thesis, Princeton University, 1995.
[5]X. Garbet and R. E. Waltz, Phys. Plasmas **3**, 1898 (1996).
[6]M. Kotschenther, W. Dorland, M. A. Beer, and G. W. Hammett, Phys. Plasmas **2**, 2381 (1995).
[7]J. A. Konings and R. E. Waltz, ''Comparisons of transport models with a transport profile database,'' to appear in Nucl. Fusion.
[8]J. L. Luxon, R. Anderson, F. Baity, C. B. Baxi, G. Bramson, N. H. Brooks, B. Brown, B. Burley, K. H. Burrel, R. W. Callis, G. L. Cambell, T. N. Carlstrom, A. P. Colleraine, J. Cummings, L. Davis, J. C. DeBoo, S. Eijima, R. Evanko, H. Fumoto, R. Gallix, J. Gilleland, T. Glad, P. Gohil, A. M. Gootgeld, R. J. Groebner, S. Hanai, J. Haskovec, E. Heckman, M. Heiberger, F. J. Helton, N. Hosogane, C.-L. Hseih, G. L. Jackson, G. Jahns, G. Janeschitz, E. Johnson, A. G. Kellman, J. S. Kim, J. Kohli, A. Langhorn, L. L. Lao, P. Leek, S. Lightner, J. Lohr, M. A. Mahdavi, M. Mayberry, B. McHarg, T. McKelvey, R. Miller, C. P. Moeller, D. Moore, A. Nerem, P. Noll, T. Ohkawa, N. Ohyabu, T. H. Osborne, D. O. Overskei, P. I. Petersen, T. Petrie, J. Phillips, R. Prater, J. Rawls, E. E. Reis, D. Remsen, P. Reidy, P. Rock, K. Schaubel, D. P. Schissel, J. T. Scoville, R. Seryadarian, M. Shimada, T. Shoji, B. Sleaford, J. P. Smith, T. Smith, R. T. Snider, R. D. Stambaugh, R. Stav, H. St. John, R. E. Stockdale, E. J. Strait, R. Stree, T. S. Taylor, J. Tooker, M. Tupper, S. K. Wong, and S. Yamaguchi, *Plasma Physics and Controlled Nuclear Fusion Research 1986* (International Atomic Energy Agency, Vienna, 1987), Vol. I, p. 159.
[9]L. L. Lao, K. H. Burrell, T. S. Casper, V. S. Chan, M. S. Chu, J. C. DeBoo, E. J. Doyle, R. D. Durst, C. B. Forest, C. M. Greenfield, R. J. Groebner, F. L. Hinton, Y. Kawano, E. A. Lazarus, Y. R. Lin-Liu, M. E. Mauel, W. H. Meyer, R. L. Miller, G. A. Navratil, T. H. Osborne, Q. Peng, C. L. Rettig, G. Rewoldt, T. L. Rhodes, B. W. Rice, D. P. Schissel, B. W. Stallard, E. J. Strait, W. M. Tang, T. S. Taylor, A. D. Turnbull, R. E. Waltz, and the DIII-D Team, Phys. Plasmas **3**, 1951 (1996).
[10]H. Rebut, V. Chuyanov, M. Huguet, R. Parker, and Y. Shimomura, in Ref. 3, Vol. 2, p. 451.
[11]J. W. Connor, M. Alexander, S. E. Attenberger, G. Bateman, D. Boucher, A. N. Chudnovskij, Yu. N. Dnestrovskij, W. Dorland, A. Fukuyama, G. T. Hoang, D. Hogeweij, W. A. Holberg, S. M. Kaye, J. E. Kinsey, J. A. Konings, M. Kotschenreuther, A. H. Kritz, V. M. Leonov, M. Marinucci, D. R. Ikkelsen, J. Ongena, A. R. Polevoi, F. Romeanelli, D. Schissel, P. M. Stubberfield, T. Takazuka, A. Taroni, M. F. Turner, G. Vlad, R. E. Waltz, and J. Weiland, ''Validation of 1-D transport models and sawteeth models for ITER,'' in *Proceedings of the 16th International Conference in Plasma Physics and Controlled Nuclear Fusion Research*, Montreal, 1996 (International Atomic Energy Agency, Vienna, in press), Paper No. IAEA-CN-64-FP-21.
[12]C. C. Petty, T. C. Luce, K. H. Burrell, S. C. Chiu, J. S. deGrasssie, C. B. Forest, P. Gohil, C. M. Greenfield, R. J. Groebner, R. W. Harvey, R. I. Pinsker, R. Prater, and R. E. Waltz, Phys. Plasmas **2**, 2342 (1995).
[13]T. O. Kingsbury and R. E. Waltz, Phys. Plasmas **1**, 2319 (1994).
[14]Y. B. Kim, P. H. Diamond, and R. J. Groebner, Phys. Fluids B **3**, 2050 (1991).
[15]T. S. Hahm and K. H. Burrell, Phys. Plasmas **2**, 1648 (1995).
[16]F. L. Hinton and G. M. Staebler, Phys. Fluids B **3**, 696 (1991).
[17]G. M. Staebler, F. L. Hinton, J. C. Wiley, R. R. Dominguez, C. M. Greenfield, P. Gohil, T. K. Kurki-Suonio, and T. H. Osborne, Phys. Plasmas **1**, 909 (1994); also G. M. Staebler, R. E. Waltz, and J. C. Wiley, Nucl. Fusion **37**, 289 (1997).
[18]G. M. Staebler, R. E. Waltz, and M. Kotschenreuther, Bull. Am. Phys. Soc. **41**, 1387 2F6 (1996).
[19]P. H. Rebut and B. E. Keen, Fusion Technol. **11**, 1 (1987).
[20]J. Hawryluk, D. Mueller, J. Hosea, C. W. Barnes, M. Beer, M. G. Bell, R. Bell, H. Biglari, M. Bitter, R. Boivin, N. L. Bretz, R. Budny, C. E. Bush, L. Chen, C. Z. Cheng, S. C. Cowley, D. S. Darrow, P. C. Efthimion, R. J. Fonck, E. Fredicksen, H. P. Furth, G. Greene, B. Grek, L. R. Grisham, G. Hammett, W. W. Heidbrink, K. W. Hill, D. Hoffmanm, R. A. Hulse, H. Hsuan, A. Janos, D. L. Jassby, F. C. Jobes, D. W. Johnson, L. C. Johnson, J. Kamperschroer, J. Kesner, C. K. Phillips, S. J. Kilpatrick, H. Kugel, P. H. Lamarche, B. LeBanc, D. M. Manos, D. K. Mansfield, E. S. Marmar, E. Mazzucato, M. P. McCarthy, J. Machuzak, M. Mauel, D. C. McCune, K. M. McGuire, S. S. Medley, D. R. Mikkelsen, D. A. Monticello, Y. Nagayama, G. A. Navratil, R. Nazikian, D. K. Owens, H. Park, W. Park, S. Paul, F. W. Perkins, S. Pitcher, D. Rasmussen, M. H. Redi, G. Rewaldt, D. Roberts, A. L. Roquemore, S. Sabbagh, G. Schilling, J. Schivell, G. L. Schmidt, S. D. Scott, J. Snips, J. Stevens, B. C. Stratton, J. D. Stratton, J. D. Sreachan, W. Stodiek, E. Synakowski, W. Tang, G. Taylor, J. Terry, J. R. Timberlake, H. H. Towner, M. Ulricksom, S. Von Goeler, R. M. Weiland, J. R. Wilson, K. L. Wong, P. Woskov, M. Ymada, K. M. Yong, M. C. Zarnstorff, and S. J. Zarnstorff, Fusion Technol. **21**, 1324 (1992).

[21]P. N. Yushmanov, T. Takizuka, K. S. Riedel, O. J. W. Kardaum, J. G. Cordey, S. M. Kaye, and D. E. Post, Nucl. Fusion **30**, 10 (1990).
[22]D. P. Schissel, in *Proceedings of the 20th European Conference*, Lisbon, 1993, Controlled Fusion and Plasma Physics (European Physical Society Petit-Lancy, 1993), Vol. 17C, Part I, p. 103; F. Ryter, O. Gruber, O. J. W. F. Kardaun, H.-P. Menzler, F. Wagner, The ASDEX-Team, the NI Group, D. P. Schissel, J. C. DeBoo, the DIII-D Research Team, S. M. Kaye, and the PBX-M Team, Nucl. Fusion, **33**, 979 (1993).
[23]R. E. Waltz, J. C. DeBoo, and M. N. Rosenbluth, Phys. Rev. Lett. **65**, 2390 (1990).
[24]C. C. Petty and T. Luce, Nucl. Fusion **37**, 2342 (1996).
[25]M. Kotchenreuther, W. Dorland, Q. P. Liu, M. A. Beer, G. W. Hammett, and S. A. Smith, ''First principles calculations of tokamak energy transport,'' in Ref. 11, Physics and Controlled Nuclear Fusion Research, Montreal, 1996, (International Atomic Energy Agency, Vienna), Paper AEA CN-64-D1-5.